Robotics and Computer–Integrated Manufacturing 49 (2018) 66–76

Contents lists available at ScienceDirect

Robotics and Computer–Integrated Manufacturing

journal homepage: www.elsevier.com/locate/rcim

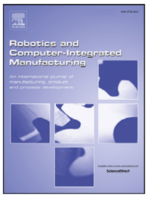

Full length Article

On a simplified nonlinear analytical model for the characterisation and design optimisation of a compliant *XY* micro-motion stage

Xavier Herpe*, Ross Walker, Matthew Dunnigan, Xianwen Kong

School of Engineering and Physical Sciences, Heriot-Watt University, Edinburgh EH14 4AS, UK

ARTICLE INFO

Keywords:
Compliant mechanism
Kinematic decoupling
PRBM
Stiffness matrix
Nonlinear analytic modelling

ABSTRACT

Compliant micro-positioning stages offer low-cost high precision and repeatability but limited workspace and nonlinear behaviour. The conventional modelling techniques used to characterise micro-motion stages are often either complex or inaccurate for large displacements. New methods have recently been developed with satisfying results. However, the presented models often focus on one part of the stage characterisation. This paper presents an analytical model used to characterise a compliant *XY* micro-motion stage in terms of stiffness and working range, taking into account the stress and buckling limitations, motion loss and parasitic displacements. The presented model combines a 6-degree-of-freedom (DOF) linear model and a simplified 2-DOF nonlinear static model. As a case study, this model is used for the design of a micro-motion stage which is intended to be the fine positioning system for a hybrid miniaturised product assembly system. The results generated by the analytical model, the finite element analysis (FEA) and the experimental testing are all in agreement. The analytical model is therefore proven to be suitable for a full characterisation and design optimisation; reducing the computation time from a few hours to a few minutes when using MATLAB rather than FEA software. Its ability to predict the output displacement as a function of the input displacement with a maximum error of less than 2% also makes it suitable for open-loop control. The travel range of the fabricated stage is greater than ±2.3 mm^2 and the maximum cross-coupling error is less than 2.5%.

1. Introduction

Due to their advantages such as compactness, cost reduction and enhanced performance, compliant *XY* motion stages are promising alternatives to conventional linear stages. They have a wide range of applications, such as fibre alignment, semi-conductor positioning, ultra-precision micromachining centres, scanners for Atomic Force Microscope (AFM) and micro-assembly [1–5]. Their inclusion in micro-motion applications has allowed for accuracy and repeatability values in the nanometre scale [2]. Compliant stages have been reported to have no backlash; no friction; no noise emission and no need for lubrication [6–8]. However, compliant *XY* motion stages also have several disadvantages which may introduce errors if neglected. Such disadvantages include: non-linear behaviour, limited working area and off-axis deviation. Serial compliant motion stages often combine two 1-DOF compliant prismatic joints which have the advantages of simple design and are naturally decoupled. However, they suffer from lower accuracy and higher inertia compared to parallel motion stages.

Clearly there is a motivation to design a low-cost 2-DOF micro-motion stage with a large workspace and a limited actuation force. Miniaturised product assembly requires micrometre scale accuracy and a range of motion at the millimetre scale. It is also desirable to have a high ratio between the first two resonant frequencies and the third one to limit unwanted displacements and minimal cross-coupling resulting in independent DOFs along the *X* and *Y* directions. Typically, parallelogram structures with flexure hinges are used in *XY* motion stages to generate translational motion.

The four main types of parallelogram structure (see [6–10] for examples) are presented in Fig. 1. The design requirements for the motion stage detailed in this paper are: the system's structural frequency is sufficiently high to avoid vibrations; the ratio between off-axis stiffness and axial stiffness is as high as possible to avoid motion along other directions and limited kinematic coupling. A multitude of *XY* motion stages have been reported in the literature [9–20], with a range of motion from $25 \times 25\ \mu\text{m}^2$ to $20 \times 20\ \text{mm}^2$, a first natural frequency between 48.3 Hz and 2.54 kHz and a coupling error between 0.5% and 5%. Micro-motion stages can be classified into two categories based on

---

* Corresponding author.
E-mail addresses: xh28@hw.ac.uk (X. Herpe), r.walker@hw.ac.uk (R. Walker), m.w.dunnigan@hw.ac.uk (M. Dunnigan), x.kong@hw.ac.uk (X. Kong).

http://dx.doi.org/10.1016/j.rcim.2017.05.012
Received 7 December 2016; Received in revised form 26 May 2017; Accepted 26 May 2017

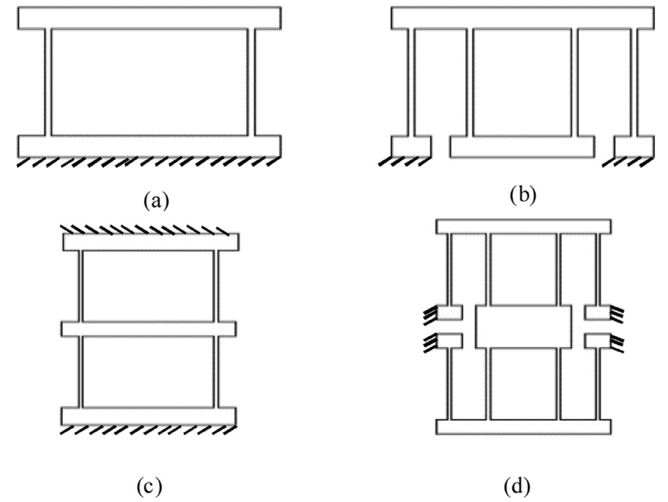

Fig. 1. Four types of parallelogram structures for micro-motion stages: (a) basic parallelogram, (b) double parallelogram, (c) compound basic parallelogram, and (d) compound double parallelogram.

the range of motion. Stages with a very short range of motion are typically very stiff, have low coupling, are compact and are often driven by piezoelectric actuators [21]. On the contrary, stages with a large range of motion are less stiff and therefore more prone to vibration, exhibit higher coupling and have a large footprint. Such stages are usually driven by Voice Coil Actuators (VCAs), or other types of electromagnetic linear actuators. To avoid cross-axis deflection and low stiffness, the *XY* motion stage designed in this paper is exclusively composed of compound basic parallelogram structures (Fig. 1(c)) with leaf-spring type flexures as in [20]. VACs are preferred to PZT actuators for their larger stroke, their ease of control and the absence of hysteresis and creep.

There are various ways to derive the stiffness matrix of a compliant stage. A commonly used modelling method is the Pseudo-Rigid Body Model (PRBM). This method, first introduced by Howell and Midha in 1994 [22], allows flexible elements to be modelled as rigid bodies connected together by torsional springs and undergoing large deflection. This method has been used to produce accurate results for small deflections [3,12,23,24].

One limitation of this method is that it often considers the compliance of the flexure joints in the direction of rotation but considers the beams as rigid bodies. Some recent models include the compression of the beams. For instance, the model derived in [12] takes into account the compression of the beams to estimate the motion loss. Based on this method, the nonlinear term induced by tension loading has been addressed to improve the model accuracy for large displacements. An extended PRBM was used in [25–27] to model compliant joints using linear springs instead of rigid links to connect the torsion springs together.

Another method commonly used is the compliance matrix method based on Hooke's law and consists of replacing each joint by an equivalent spring model. This method has been reported to be accurate and efficient for small displacements [6,7,11,13,15,17,28–32] and is often used as it allows for a full analysis of deformation of all links. Simplification of the compliance matrix is usually achieved by reducing the number of DOFs of the flexures from 6 to 3 in the analysis. This method is efficient but has limitations when larger displacements are applied with reported errors of 7.4% in [33], 8.5% in [7], 10% in [15] and 20% in [6].

Basic derivations based on elastic theory are limited to mechanisms with a simple structure, but is probably the simplest method and is sufficient in many cases [18,34–37]. However, as the previous method, this method is only efficient for small displacements. This has been documented in [18] and [34], where the displacement error reaches 30.9% and 9% respectively when compared to FEA.

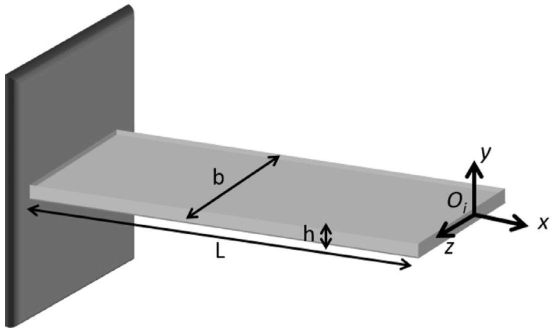

Fig. 2. Beam dimensional parameters.

Alternatively, [9,38–41] derived a nonlinear force-displacement relationship based on equations established in [42] for beam-based mechanisms using a Beam Constraint Model (BCM). The model used takes into account the load stiffening phenomena with very large axial forces for a motion range of up to 10% of the beam's length. This model is regarded as an efficient analytical method but the introduction of tension in the beams could be simplified.

Using elliptic integrals to model large deflection of beams is considered the most accurate technique as explained in [43]. However, this method requires time consuming complex calculations. This paper presents an extensive analytical model used to design, optimise and fabricate an *XY*-stage with a simple structure.

The proposed model is an alternative to the PRBM and the BCM methods. It uses simple, well established, beam bending equations and basic geometric properties to integrate the nonlinearities caused by large displacements, such as tension loading. The analytical model combines a 6-DOF linear stiffness matrix to characterise the frequency response and a 2-DOF nonlinear model to characterise the nonlinear stiffness and the workspace of the *XY* motion stage. The impact of dimensional parameters on the stiffness and travel range is evaluated and the model is implemented in MATLAB to perform design optimisation. A compliant *XY* stage is then fabricated based on the optimisation results. Finally, FEA and experimental tests are compared to the analytical model for validation. While other models may accurately predict the nonlinear deformation of beams in parallelogram structures, this model allows for a full characterisation of the *XY* stage, including cross-coupling, motion loss and travel range with both nonlinear stress and buckling taken into account. This model can be used as a reliable design tool for any parallelogram structure but can also be included in the control system of an *XY* motion stage to compensate the displacement errors and allow for open-loop control.

2. Modelling

Defining the stiffness of the compliant stage determines the relationship between the input displacement, the actuation force and the resonant frequencies, while the maximum stress and the buckling point determine the range of motion.

2.1. Stiffness matrix

Firstly, a stiffness matrix is derived to create a dynamic model of the stage. A 6-DOF representation allows the model to be used for a wide range of applications. The main purpose of the stiffness matrix in this study is to calculate the resonant frequencies of the stage. It will also be used for comparison with the nonlinear model, FEA and experimental test results.

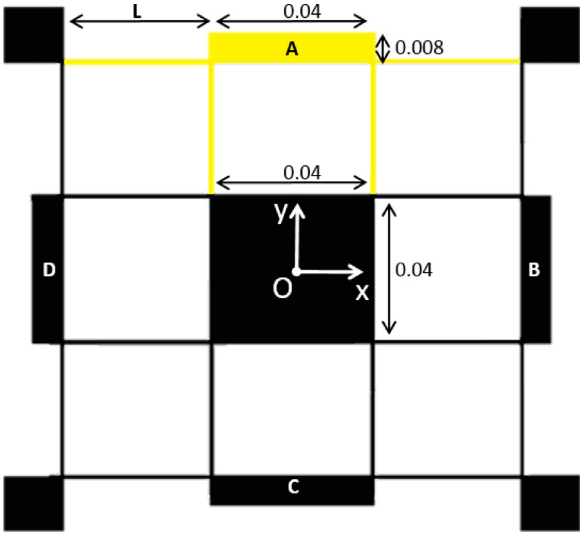

Fig. 3. Schematic top view of the compliant *XY* motion stage. (For interpretation of the references to colour in this figure legend, the reader is referred to the web version of this article.)

2.1.1. General beam modelling and transformation

The dimensional parameters of a beam are presented in Fig. 2 and the dimensions of the *XY* motion stage are shown in Fig. 3. The dimensions are given in metre and all the beams have the same dimensions.

The static equation of the beam presented in Fig. 2 can be written as in [13] and [44]:

$$\underline{F} = K_{fix_g}.\underline{X} \tag{1}$$

where $\underline{F}$ is a vector representing the forces and moments applied at the end of the beam, K_{fix_g} is the stiffness matrix of the beam with fixed-guided boundary conditions and $\underline{X}$ is a vector representing the translations and rotations at the end of the beam. The stiffness matrix of the fixed-guided beam is:

$$\begin{pmatrix} F_x \\ F_y \\ F_z \\ M_x \\ M_y \\ M_z \end{pmatrix} = \begin{bmatrix} \frac{EA}{L} & 0 & 0 & 0 & 0 & 0 \\ 0 & \frac{12EI_z}{L^3} & 0 & 0 & 0 & \frac{6EI_z}{L^2} \\ 0 & 0 & \frac{12EI_y}{L^3} & 0 & -\frac{6EI_y}{L^2} & 0 \\ 0 & 0 & 0 & \frac{GJ}{L} & 0 & 0 \\ 0 & 0 & -\frac{6EI_y}{L^2} & 0 & \frac{4EI_y}{L} & 0 \\ 0 & \frac{6EI_z}{L^2} & 0 & 0 & 0 & \frac{4EI_z}{L} \end{bmatrix} \begin{pmatrix} \delta_x \\ \delta_y \\ \delta_z \\ \theta_x \\ \theta_y \\ \theta_z \end{pmatrix} \tag{2}$$

where F_n and δ_n are the force and translation along the *n* axis, M_n and θ_n are the moment and displacement around the *n* axis, *E* is the Young's modulus, *G* is the shear modulus, *A* is the area of the beam's cross section, *L* is the length of the beam, *J* is the torsion constant and I_y and I_z are the area moments.

The stiffness of a beam can be shifted from its local coordinate system to a general coordinate system by using the shifting law from screw theory and the work reported in [6,28,44]. This process involves pre-multiplying the stiffness matrix in coordinate O_i by the inverse transpose of the adjoint transformation matrix and then multiplying it by the inverse of the adjoint transformation matrix, as shown below:

$$K_i^j = T_i^{j^{-T}} \cdot K_i \cdot T_i^{j^{-1}} \tag{3}$$

where *i* represents the local coordinate system of the beam and *j* represents the coordinate system in which the beam's stiffness is shifted. The adjoint transformation matrix T_i^j is:

$$T_i^j = \begin{bmatrix} R_i^j & S\left(p_i^j\right).R_i^j \\ 0 & R_i^j \end{bmatrix} \tag{4}$$

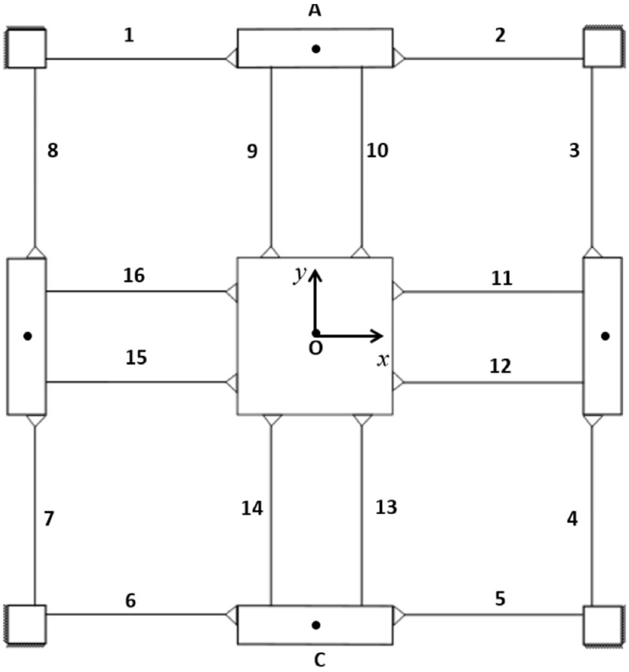

Fig. 4. Nonlinear spring-equivalent model of the *XY* stage.

where R_i^j represents the rotation matrix of O_i relative to O_j and $S(p_i^j)$ represents the skew symmetric operator for the vector $p_i^j = |p_x, p_y, p_z|$, denoted as:

$$S\left(p_i^j\right) = \begin{bmatrix} 0 & -p_z & p_y \\ p_z & 0 & -p_x \\ -p_y & p_x & 0 \end{bmatrix} \tag{5}$$

The rotation matrix R_i^j is obtained by multiplying the rotation matrices around each axis:

$$R_i^j = Rx_i^j.Ry_i^j.Rz_i^j \tag{6}$$

where Rx_i^j, Ry_i^j and Rz_i^jrepresent the 3×3 rotation matrices around the *X*-, *Y*- and *Z*-axes by angles ϕ, Ψ and θ, respectively.

2.1.2. Individual parallelogram modules stiffness

Due to the symmetry of the design, the overall stiffness can be obtained by only deriving the stiffness of the top quarter composed of beams 1, 2, 9 and 10 (highlighted in yellow in Fig. 3). The beam numbers can be found in Fig. 4.

Firstly, the stiffness of the parallelogram *A*, composed of the beams 1 and 2, is represented at point *O*. The stiffness of beam 1 at point *O* is obtained by a pure translation along the *X*- and *Y*-axes, giving:

$$K_1^O = T_1^{O-T} \cdot K_1 \cdot T_1^{O-1} \tag{7}$$

with $K_1 = K_{fix\_g}$ and $p_1^O = |0.02,\ -(L+0.02),\ 0|$. Since beams 1 and 2 are symmetric about the *Y*-axis, the stiffness of beam 2 at point *O* is by rotating beam 1 around the *Y*-axis by π radians:

$$K_2^O = Ry(\pi)_2^{O-T} \cdot K_1^O \cdot Ry(\pi)_2^{O-1} \tag{8}$$

The stiffness of beam 9 at point *O* is obtained by rotating the initial beam stiffness matrix by $-\pi/2$ around the *Z*-axis and translating by $p_9^O = |0.02,\ -0.02,\ 0|$:

$$K_9^O = T_9^{O-T} \cdot K_{fix\_g} \cdot T_9^{O-1} \tag{9}$$

Since beams 9 and 10 are symmetric about the *Y*-axis, the stiffness of beam 10 at point *O* is obtained by rotating beam 9 around the *Y*-axis by π radians:

$$K_{10}^O = Ry(\pi)_2^{O-T} \cdot K_9^O \cdot Ry(\pi)_2^{O-1} \tag{10}$$

The beams 1 and 2 are in a parallel configuration with the parallelogram A and the beams 9 and 10 are in a parallel configuration with the centre of the stage O. The pairs of beams 1–2 and 9–10 are in a serial configuration with the centre of the stage O. Therefore, the stiffness of the top quarter of the stage at point O is:

$$K_{O1} = \frac{1}{\left(K_1^O + K_2^O\right)^{-1} + \left(K_9^O + K_{10}^O\right)^{-1}} \tag{11}$$

2.1.3. *Stiffness of the* XY *motion stage*

The stiffness of the remaining three quarters is obtained by successively rotating K_{O1} three times by $-\pi/2$ around the Z-axis as follows:

$$K_{O2} = Rz\left(-\frac{\pi}{2}\right)_O^{-T} \cdot K_{O1} \cdot Rz\left(-\frac{\pi}{2}\right)_O^{-1} \tag{12}$$

$$K_{O3} = Rz\left(-\frac{\pi}{2}\right)_O^{-T} \cdot K_{O2} \cdot Rz\left(-\frac{\pi}{2}\right)_O^{-1} \tag{13}$$

$$K_{O4} = Rz\left(-\frac{\pi}{2}\right)_O^{-T} \cdot K_{O3} \cdot Rz\left(-\frac{\pi}{2}\right)_O^{-1} \tag{14}$$

with K_{O2}, K_{O3} and K_{O4} representing the stiffness of the groups of beams 3–4–11–12, 5–6–13–14 and 7–8–15–16 at point O respectively. The stiffness matrix of the whole XY stage K is therefore:

$$K = K_{O1} + K_{O2} + K_{O3} + K_{O4} \tag{15}$$

2.2. *Nonlinear model*

Linear beam bending assumes an unchanged beam's length. However, this is not valid for large deflections. This is why a nonlinear model is derived by including the nonlinear term induced by tension loading of the beams. In deriving the nonlinear modelling of the micro-motion stage (Fig. 4), two types of compliant structure are analysed: the outer parallelogram structure (beams 1–8) and the inner parallelogram structure (beams 9–16). All the beams are represented as linear-elastic elements connected to rigid bodies. In order to simplify the model, several assumptions have to be made. Firstly, parallelograms A and C can only translate along the Y-axis and parallelograms B and D can only translate along the X-axis.

From these assumptions, the following boundary conditions can be established:

$$\begin{cases} \delta_{Ay} = \delta_{1y} = \delta_{2y} \\ \delta_{Cy} = \delta_{5y} = \delta_{6y} \\ \delta_{Bx} = \delta_{3x} = \delta_{4x} \\ \delta_{Dx} = \delta_{7x} = \delta_{8x} \end{cases} \tag{16}$$

where δ_{Ay} represents the displacement of point A along the Y-axis, δ_{1y} represents the displacement of beam 1 along the Y-axis and so on. As a consequence of the previous assumption, the following is clear:

$$\begin{cases} F_{Ay} = F_{1y} + F_{2y} \\ F_{Cy} = F_{5y} + F_{6y} \\ F_{Bx} = F_{3x} + F_{4x} \\ F_{Dx} = F_{7x} + F_{8x} \end{cases} \tag{17}$$

where F_{Ay} represents the reaction force of the parallelogram A for an input displacement δ_{Ay}, F_{1y} represents the reaction force of the beam 1 for an input displacement δ_{1y} and so on.

2.2.1. *Outer parallelogram*

The total stiffness of one outer parallelogram structure can be obtained from the modelling of a single beam (Fig. 5). In this model, the stiffness due to bending is combined with the stiffness induced by tension.

Effect of bending: As in [45], the force F_{1y_bend} acting downwards due to the bending of the beam can be expressed as:

$$F_{1y\_bend} = \frac{12EI_z\delta_{1y}}{{L_1}^3} \tag{18}$$

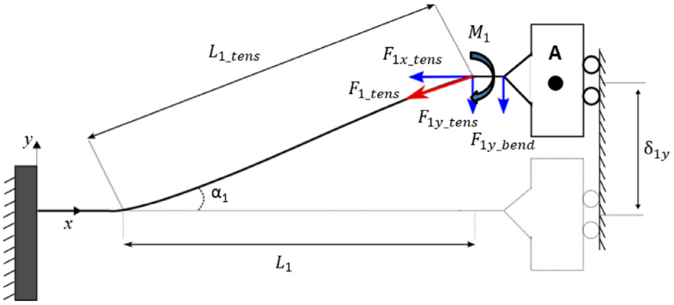

Fig. 5. Spring-equivalent model of a beam.

where E is the Young's modulus, I_z is the area moment of inertia and L_1 is the initial length of beam 1.

Effect of tension: In the tension analysis, bending is ignored and the beam is regarded as a linear spring connected at both ends by frictionless revolute joints. It is known that the stress induced by tension loading is given by:

$$\sigma_{1\_tens} = \varepsilon_1 E = \frac{F_{1\_tens}}{A} \tag{19}$$

where σ_{1_tens} is the stress generated by pure tension loading on beam 1, ε is the strain on beam 1, A is the cross-sectional area of the beam and F_{1_tens} is the tension load applied to beam 1.

The length of the beam after being stretched is approximated using Pythagoras theorem:

$$L_{1\_tens} = \sqrt{{L_1}^2 + {\delta_{1y}}^2} \tag{20}$$

where L_{1_tens} represents the elongated length of beam 1 and L_1 represents the initial length of beam 1. The value of the strain ε_1 is then:

$$\varepsilon_1 = \frac{\Delta L_1}{L_1} = \frac{L_{1\_tens} - L_1}{L_1} \tag{21}$$

The relationship between the tension force F_{1_tens} and the resulting force F_{1y_tens} acting downwards is given by:

$$F_{1y\_tens} = F_{1\_tens} \sin\alpha_1 \tag{22}$$

with:

$$\alpha_1 = \tan^{-1}\left(\frac{\delta_{1y}}{L_1}\right) \tag{23}$$

Rearranging Eqs. (19)–(23), the force due to tension is:

$$F_{1y\_tens} = EA\varepsilon_1 \sin\alpha_1 \tag{24}$$

From Eqs. (18) and (24), the total force applied by beam 1 acting along the Y-axis is therefore:

$$F_{1y} = F_{1y\_bend} + F_{1y\_tens} \tag{25}$$

2.2.2. *Inner parallelogram*

Because of the symmetrical boundary conditions, the total stiffness of one inner parallelogram structure (for instance beams 15 and 16) can be derived from a single beam coupled to one half of the outer parallelogram structure linked to it (Fig. 6). The stiffness K_{16} of the beam 16 along the X-axis is given by:

$$K_{16x} = \frac{EA}{L_{16}} \cos\alpha_{16} \tag{26}$$

For small angles, the following approximation can be made:

$$K_{16x} \approx \frac{EA}{L_{16}} \tag{27}$$

The stiffness of beam 8 along the X-axis K_{8x} is derived as follows: firstly, the stiffness due to bending is:

$$K_{8x\_bend} = \frac{12EI_z}{{L_8}^3} \tag{28}$$

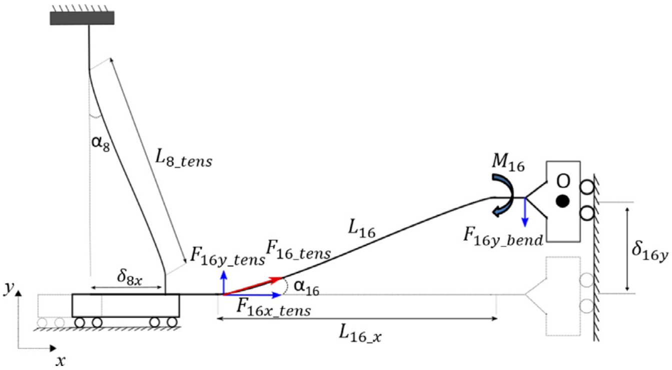

Fig. 6. Spring-equivalent model of orthogonal beam configuration.

Then, the stiffness due to tension is:

$$K_{8x\_tens} = \frac{EA}{L_8}\sin\alpha_8 \tag{29}$$

Therefore, the total resulting stiffness of beam 8 along the X-axis is:

$$K_{8x} = K_{8x\_bend} + K_{8x\_tens} \tag{30}$$

For a small displacement δ_{16} and therefore a very small displacement δ_8 and angle α_8, it is observed that:

$$K_{8x} \ll K_{16x} \tag{31}$$

From this observation and to simplify the model, the change in axial deformation of the beams of the inner parallelogram is neglected in this part. It will be included later for motion loss compensation. The projection of beam 16 along the X-axis is:

$$L_{16\_x} = \sqrt{L_{16}{}^2 - \delta_{16}{}^2} \tag{32}$$

The deflection of beam 8 can be obtained as follows:

$$\delta_{8x} = L_{16} - L_{16\_x} \tag{33}$$

Taking all these simplifications into account, the calculation of the relationship between δ_{8x} and F_{16y} can be determined. Based on Eq. (25), the force acting along the X-axis is:

$$F_{16x\_tens} = \frac{12EI_z}{L_8{}^3}\delta_{8x} + \frac{EA}{L_8}\Delta L_8 \sin\alpha_8 \tag{34}$$

The force acting along the Y-axis is therefore a combination of the forces applied by beams 8 and 16:

$$F_{16y} = \frac{F_{16x\_tens}\delta_{16y}}{L_{16\_x}} + \frac{12EI_z\delta_{16y}}{L_{16}{}^3} \tag{35}$$

2.2.3. Force-displacement model of the motion stage

All the beams have the same initial length L. From the preliminary assumptions, the boundary conditions and the above derivations, the position of each outer parallelogram can be related to the position of the centre O as follows:

$$\delta_{Ay} = \delta_{Oy} - \left(L - \sqrt{L^2 - \delta_{Ox}{}^2}\right) \tag{36}$$

$$\delta_{Cy} = \delta_{Oy} + \left(L - \sqrt{L^2 - \delta_{Ox}{}^2}\right) \tag{37}$$

$$\delta_{Bx} = \delta_{Ox} - \left(L - \sqrt{L^2 - \delta_{Oy}{}^2}\right) \tag{38}$$

$$\delta_{Dx} = \delta_{Ox} + \left(L - \sqrt{L^2 - \delta_{Oy}{}^2}\right) \tag{39}$$

Using Eqs. (25) and (35), the reaction forces at point O along the X- and the Y-axes required to move the motion stage by δ_{Ox} and δ_{Oy} are:

$$\begin{cases} F_{Ox} = F_{Bx} + F_{Dx} + F_{9x} + F_{10x} + F_{13x} + F_{14x} \\ F_{Oy} = F_{Ay} + F_{Cy} + F_{11y} + F_{12y} + F_{15y} + F_{16y} \end{cases} \tag{40}$$

It is assumed that the sum of the reaction forces along the X-axis is unchanged when represented at points B, D or O, and the sum of the forces along the Y-axis is unchanged when represented at points A, C or O.

2.2.4. Motion loss compensation

The simplified nonlinear model presented in this section assumes that the input displacements are applied at the centre of the stage (i.e. point O). This means that the desired output displacements are simply equal to the input displacements. In reality, the input displacements are applied by two actuators at point D along the X-axis and at point C along Y-axis, causing the output displacements at point O to be different.

The first element causing a difference between the input and the output displacements is the compression of the inner beams. Based on the work from [12] and using Eq. (19), the positioning error at point O along the X-axis error caused by the compression of beams 15 and 16 can be approximated as follows:

$$\delta_{Ox\_com} = \frac{L\left(F_{Bx} + F_{9x} + F_{10x} + F_{13x} + F_{14x}\right)}{2EA} \tag{41}$$

Similarly, the positioning error at point O along the Y-axis caused by the compression of beams 13 and 14 is:

$$\delta_{Oy\_com} = \frac{L\left(F_{Ay} + F_{19y} + F_{20y} + F_{23y} + F_{24y}\right)}{2EA} \tag{42}$$

The second source of error is the parasitic displacement caused by the constrained positions of parallelograms C and D, also called cross-coupling. The parasitic displacement along the X-axis can be estimated by calculating the difference between the desired output displacement δ_{Ox} and the resulting displacement δ_{Dx} of parallelogram D:

$$\delta_{Ox\_par} = \delta_{Ox} - \delta_{Dx} \tag{43}$$

Similarly, the parasitic displacement along the Y-axis can be estimated by calculating the difference between the input displacement δ_{Oy} and the resulting displacement δ_{Cy} of parallelogram C:

$$\delta_{Oy\_par} = \delta_{Oy} - \delta_{Cx} \tag{44}$$

Therefore, the corrected output displacement at point O along the X-axis is:

$$\delta_{Ox\_corrected} = \delta_{Ox} - \delta_{Ox\_com} + \delta_{Ox\_par} \tag{45}$$

and the corrected output displacement at point O along the Y-axis is:

$$\delta_{Oy\_corrected} = \delta_{Oy} - \delta_{Oy\_com} + \delta_{Oy\_par} \tag{46}$$

2.3. Stress analysis

A nonlinear stress analysis is carried out to define the maximum allowable displacement of the XY motion stage, which is directly linked to the yield strength of the material. The maximum stress due to bending occurs at one end of the outer parallelogram beams at the cross-section's farthest edge from the neutral axis. It is given by:

$$\sigma_{1\_bend} = \frac{M_1 c}{I} \tag{47}$$

where c is the distance from the neutral axis, or half of the beam's thickness h in this case, and $M_1 = F_{1y\_bend} \times 0.5 \times L_1$. Combining Eqs. (18) and (47), the maximum stress due to bending is:

$$\sigma_{1\_bend} = \frac{3Eh\delta_{1y}}{L_1{}^2} \tag{48}$$

Adding the stress induced by tension loading from Eq. (19), the maximum stress is given by:

$$\sigma_1 = K1 \cdot \sigma_{1\_bend} + K2 \cdot \sigma_{1\_tens} \tag{49}$$

where $K1$ and $K2$ denote the stress concentration factors for the stress due to bending and the stress due to tension respectively. These coefficients will be defined later in this paper.

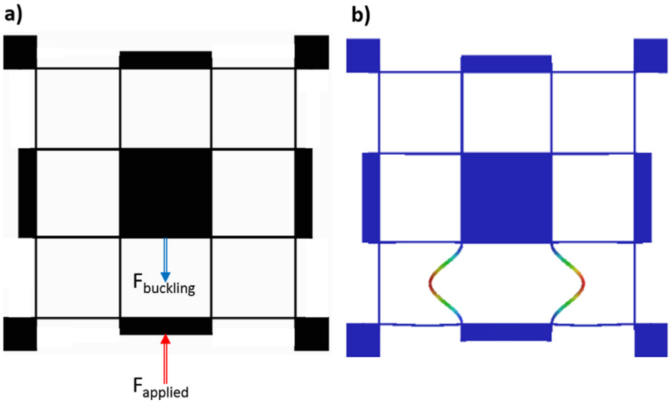

Fig. 7. Buckling: (a) force diagram, (b) FEA result.

2.4. Buckling analysis

Most of the existing work on compliant *XY* stages only uses the yield strength as a travel range limitation. For short and thick beams, the force required to cause buckling is often much higher than the force required to reach a stress equal to the material yield strength. However, for longer and thinner beams, buckling can occur before the yield strength is reached and cannot be ignored. Therefore, the buckling point of the beams is integrated in this study. From [46], the critical point of a beam fixed at both ends is given by:

$$F_{crit} = \frac{4\pi^2 E I_z}{L^2} \tag{50}$$

Buckling should occur at one of the inner beams parallel to the loading direction and where the reaction force is the highest. Since there are only sets of two beams, it is assumed that the buckling force is twice F_{crit}. When a force $F_{applied}$ is applied at the bottom of the stage (Fig. 7(a)), the reaction force $F_{buckling}$ acting on the set of beams is obtained by subtracting the reaction force of parallelogram C from the reaction force of the whole stage along the same direction. It is assumed that buckling occurs for a large input displacement, when the nonlinear term induced by tension loading becomes much higher than the linear term. Comparing Eqs. (25) and (35), if an input displacement is applied at point *C* along *Y* direction, the larger the displacement, the more insignificant becomes the reaction forces caused by the inner beams compared to the reaction forces from parallelograms *A* and *C*. Thus, the buckling force $F_{buckling}$ is approximately 1/2 of the force applied at the bottom of the *XY* stage $F_{applied}$. The input force required to cause buckling is therefore given by:

$$F_{applied} = \frac{16\pi^2 E I}{L^2} \tag{51}$$

3. Dynamic analysis

A dynamic analysis is carried out to calculate the resonant frequencies of the six mode shapes. Applying Newton's second law, the system undamped equation of motion can be expressed as:

$$M\underline{\ddot{x}} + K\underline{x} = 0 \tag{52}$$

where *M* and *K* correspond to the system's mass matrix and stiffness matrix respectively and $\underline{x}$ is a vector representing the motion in the Cartesian coordinate system. The mass matrix is defined as:

$$M = \begin{bmatrix} M_{xx} & 0 & 0 & 0 & 0 & 0 \\ 0 & M_{yy} & 0 & 0 & 0 & 0 \\ 0 & 0 & M_{zz} & 0 & 0 & 0 \\ 0 & 0 & 0 & I_{xx} & 0 & 0 \\ 0 & 0 & 0 & 0 & I_{yy} & 0 \\ 0 & 0 & 0 & 0 & 0 & I_{zz} \end{bmatrix} \tag{53}$$

Table 1
Masses of a beam, inner, and outer parallelogram.

Parameters	m_O	m_p	m_{beam}
Mass (10^{-3} kg)	$0.04^2 \times b \times \rho$	$0.04 \times 0.008 \times b \times \rho$	$b \times h \times L \times \rho$

where M_{xx}, M_{yy} and M_{zz} represent the moving mass of the stage along the *X*-, *Y*- and *Z*-axes respectively and I_{xx},I_{yy} and I_{zz} represent the moment of inertia of the stage around the *X*-, *Y*- and *Z*-axes respectively:

$$M_{xx} = M_{yy} = m_O + 2m_p + \left(8 \times \frac{33}{140} m_{beam}\right) + (4 \times m_{beam}) \tag{54}$$

$$M_{zz} = m_O + \left(8 \times \frac{33}{140} m_{beam}\right) \tag{55}$$

$$I_{xx} = I_{yy} = \frac{m_o(0.04^2 + b^2)}{12} + 2m_p\left(\frac{0.008^2 + b^2}{12} + (L + 0.02)^2 + \frac{(0.04^2 + b^2)}{12}\right) \tag{56}$$

$$I_{zz} = 4m_p\left(\frac{0.04^2 + 0.008^2}{12}\right) + m_o\left(\frac{0.04^2 + 0.04^2}{12}\right) \tag{57}$$

The masses used in the mass matrix are listed in Table 1. m_{beam} is the mass of a single beam. According to [47], the lumped mass equivalent of a bending beam can be represented as a massless beam with a mass located at its free end with the value of $33/140 \times m_{beam}$. m_o represents the mass of parallelogram *O* and m_p represents the mass of each outer parallelograms (i.e. *A, B, C* and *D*).

Based on vibration theory, the mode equation can be written as:

$$(M^{-1}K - \omega^2 I)X = 0 \tag{58}$$

where *X* is a matrix representing the mode shapes, ω is it a vector representing the corresponding angular natural frequencies and *I* is the identity matrix. The natural frequencies are then given by:

$$f_i = \frac{1}{2\pi}\omega_i \tag{59}$$

where f_i represents the natural frequency of the i^{th} *i*th mode.

4. Design optimisation

Using the analytical model presented in Sections 2 and 3 rather than FEA enables quick design synthesis and a quick insight on parameters due to its high flexibility. The four properties on which this study is focused are: the resonant frequencies of the first two modes, these should occur equally along the *X*- and the *Y*-axes; the third resonant frequency; the maximum allowable displacement and the corresponding force input requirement. The maximum displacement is defined using the yield strength of the material and the buckling point of the beams. Coupling and motion loss are ignored in this section because their impact on the beam dimensions is negligible.

In the first instance, the beam thickness (*h*), height (*b*) and length (*L*) are varied from 0.5 mm to 1 mm, 5 mm to 10 mm and 20 mm to 50 mm, respectively. This allows for an overview of the effect of dimensional parameters on the stage's behaviour. The equations resulting from the analytical model are therefore implemented in MATLAB and the results are shown in Fig. 8. Aluminium 7075-T6 is selected as it has a large reversible strain and is widely used for this application. The material properties are listed in Table 2. A few observations can be made. First of all, increasing the length of the beams will increase the maximum allowable displacement. However, this will also reduce the resonant frequencies. Increasing the height of the beams results in an increased third resonant frequency without affecting the range of motion. However, the force input requirement is also increased. Finally, increasing the thickness of the beams will increase the resonant

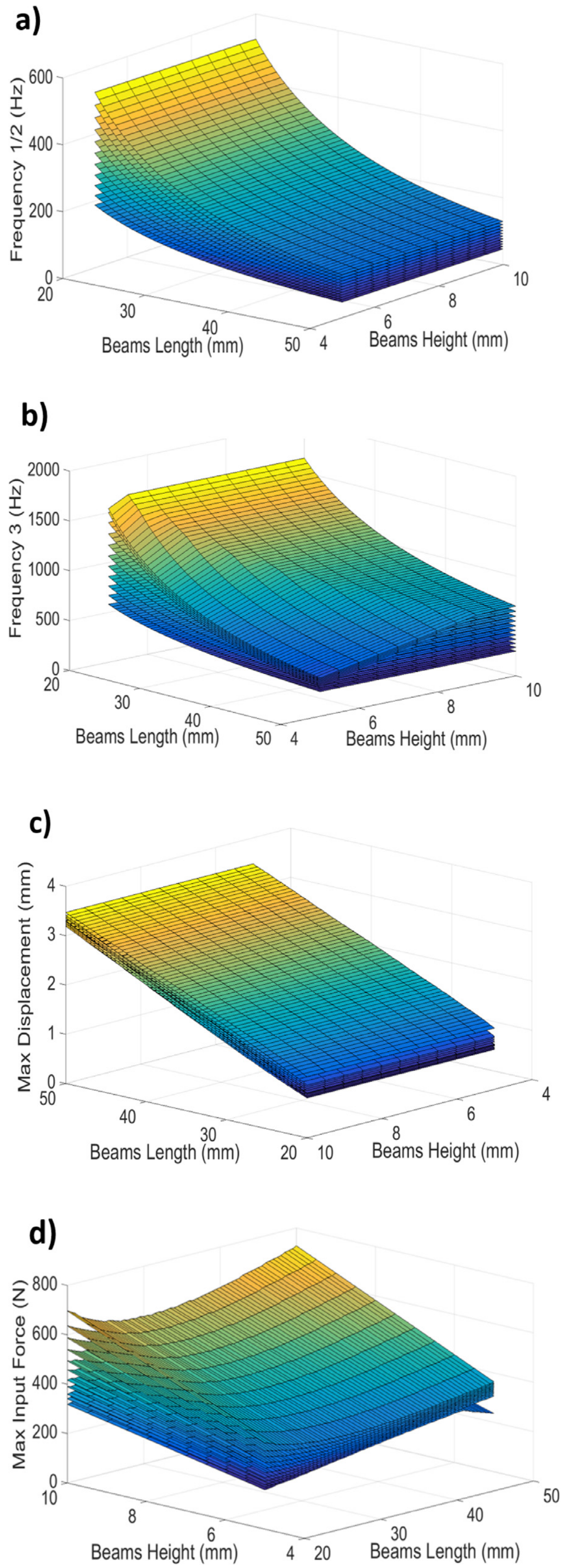

Fig. 8. Properties of the stage as a function of the width and length of the beams: (a) first and second resonant frequencies, (b) third resonant frequency, (c) maximum displacement, (d) input force.

Table 2
Parameters of the *XY* motion stage.

Parameters	b (m)	h (m)	L (m)	E (Pa)	G (Pa)	ρ (kg/m^3)
Values	0.006	0.0005	0.045	71,7e^9	26,9e^9	2810

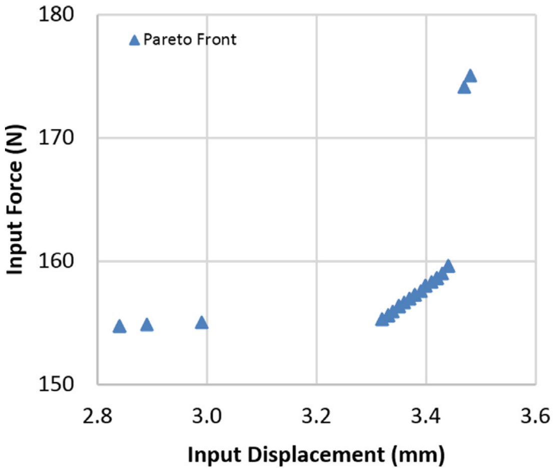

Fig. 9. Pareto front.

frequencies along the three axes but will reduce the range of motion and increase the force input requirement. These observations comply with the results found in the literature for similar structures.

Optimisation of PRBM parameters was proposed in [27] and allows the user to find which model is the most suitable for a given design. However, it does not optimise the beams' dimensions to achieve a specific goal. Design optimisation using genetic algorithms (GAs) [3,48,49] or other techniques such as particle swarm optimisation (PSO) [6,10] is commonly used for compliant stages but the presented models do not include the nonlinearities induced by tension, making them only suitable for small displacements.

In this study, design optimisation is performed using a multi-objective GA to obtain a Pareto optimal solution set in MATLAB. The design objectives are to maximise the range of motion and minimise the required input force while keeping the resonant frequencies as high as possible. The design constraints applied are:

- Resonant frequencies f_1 and $f_2 > 50$ Hz.
- Minimum frequency ratio $f_1/f_3 > 1/3$.
- Maximum stress $\sigma_{max} < 505$ MPa.
- Maximum input $F_{Ox} < F_{applied}$, corresponding to the buckling point.

The parameters ranges are:

- $b = 6$ mm (manufacturing constraint)
- 0.5 mm $< h < 1$ mm
- 20 mm $< L < 50$ mm.

The Pareto optimal set is presented in Fig. 9. For each point on the Pareto front corresponds a set of beam parameters. The rounded dimensions selected for this study are shown in Table 2. Applying a safety factor of 1.5 on the maximum stress and limiting the required input force to 68 N, these dimensions allow for an input displacement of up to ±2.3 mm along both directions.

The average computation time for the MATLAB program to run on a standard computer (Intel® i5 3.2 GHz processor, 4GB RAM) is less than 140 s to cover more than 26,000 combinations. This algorithm is therefore proven to significantly improve the efficiency of the design and evaluation of the appropriate dimensional parameters of the micro-motion stage. This tool can be used to characterise the *XY* motion stage in terms of working area and stiffness and can be used to select the appropriate dimensional parameters of the beams and actuators.

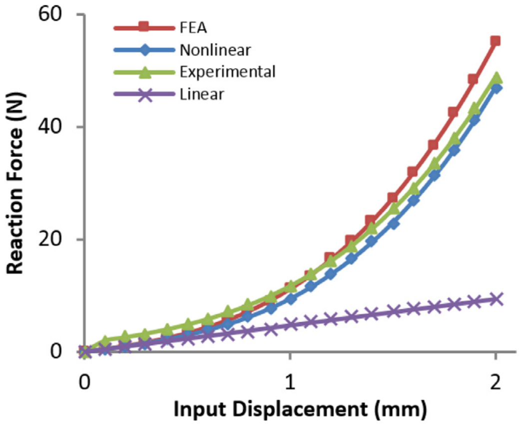

Fig. 10. Stiffness along a single direction.

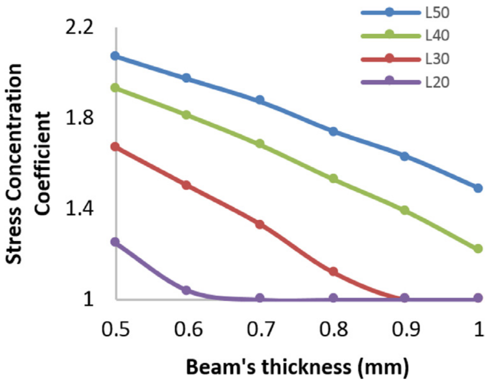

Fig. 11. Stress concentration coefficients in function of the beam's thickness and length.

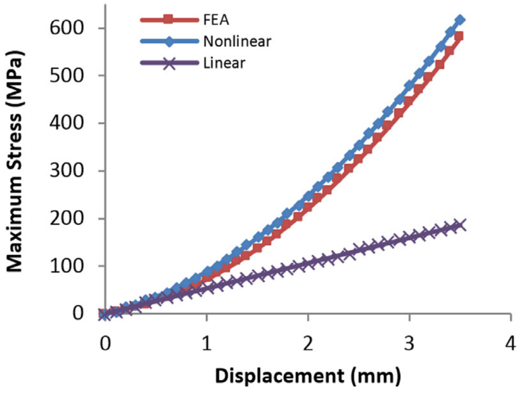

Fig. 12. Stress analysis: linear and nonlinear models compared with FEA.

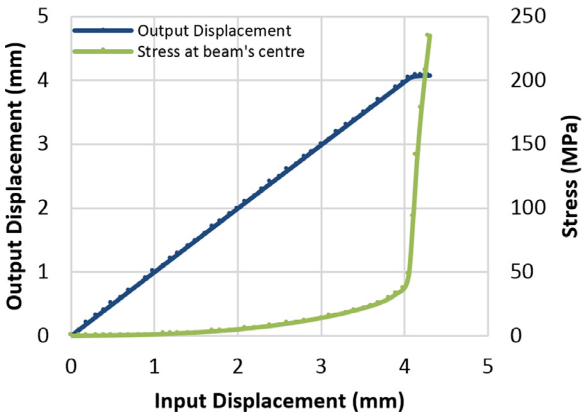

Fig. 13. Stress and output displacement response to a large input displacement.

5. FEA validation

In order to validate the analytical model, nonlinear FEA is carried out using ABAQUS with the dimensions and properties listed in Table 2. In order to reduce the stress concentration, corners of 0.5 mm radius have been added at both ends of the beams.

5.1. Force-displacement analysis

To study the force-displacement relationship, an input displacement of 2 mm is gradually applied along the X-axis (i.e. point D) and the reaction force is recorded. The results are then compared with the analytical linear (Eq. (15)) and nonlinear (Eq. (40)) models (Fig. 10). These results clearly show that although some linear behaviour can be observed between 0 and 0.5 mm, the load stiffening phenomena induces significant nonlinearities for large displacements. The accuracy of the stiffness matrix method is therefore limited to very small range. However, the maximum error of the nonlinear model is 16.2% at 1.3 mm, corresponding to only 3.2 N. The efficiency of the nonlinear terms added to the analytical model to define the stiffness is therefore validated.

5.2. Stress analysis

In order to define the stress concentration factors $K1$ and $K2$ for Eq. (49), an FEA analysis is carried out on beams of length between 20 mm and 50 mm and thickness between 0.5 mm and 1 mm, with a constant corner radius of 0.5 mm. For each combination, the resulting stress is plotted against the input displacement and MATLAB is used to fit the curve to Eq. (49) using the nonlinear least squares method. The results of this analysis are shown in Fig. 11 because $K1$ and $K2$ cannot be lower than 1, the coefficient $K2$ is constantly 1 and $K1$ varies between 1 and 2.10. The stress concentration factor $K1$ of the designed XY motion stage, obtained by linear interpolation, is 2. The FEA results show that the yield strength is reached for an input displacement of 3.24 mm (Fig. 12). The yield strength is reached at 3.1 mm for the nonlinear model and at 9.51 mm for the linear model. The maximum input displacement given by the analytical model is therefore 4.3% smaller than FEA. As for the force-displacement analysis, it is clearly shown that the nonlinear model can also efficiently integrate nonlinear stress as a travel range limitation.

5.3. Buckling analysis

The buckling point is estimated from the FEA results by analysing the output data for a large displacement. Buckling is occurring when the stress at the centre of the inner beams increases suddenly and the difference between the input and the output displacement of the stage increases significantly. From Fig. 13, the buckling point is estimated to occur when the input displacement is around 4.05 mm, corresponding to an input force of 351.3 N. The buckling point obtained from the nonlinear model (Eq. (51)) gives an input force of 349.5 N, corresponding to an input displacement of 4.13 mm. The error between FEA and the nonlinear model is therefore 0.5%.

5.4. Coupling analysis

A coupling analysis is carried out to estimate the maximum positioning error and evaluate the capability of the analytical model to predict this error. The maximum error is assumed to occur when the maximum input displacements are applied simultaneously along the X- and the Y-axes.

First, an input displacement of 2.2 mm is applied at point C along the Y-axis, as presented in Fig. 14. The parasitic output displacement

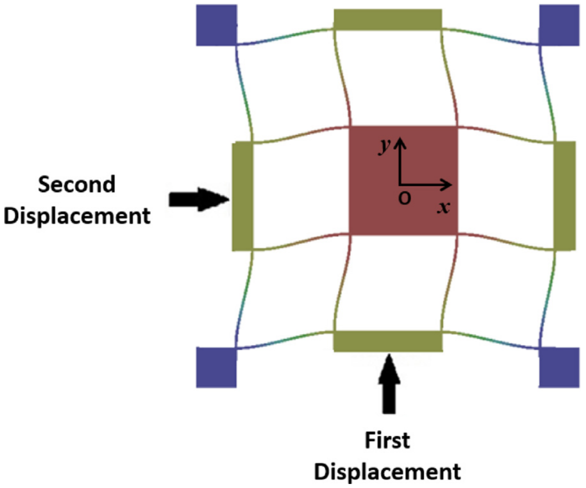

Fig. 14. Deformed *XY* stage with input displacement applied along *X* and *Y* directions.

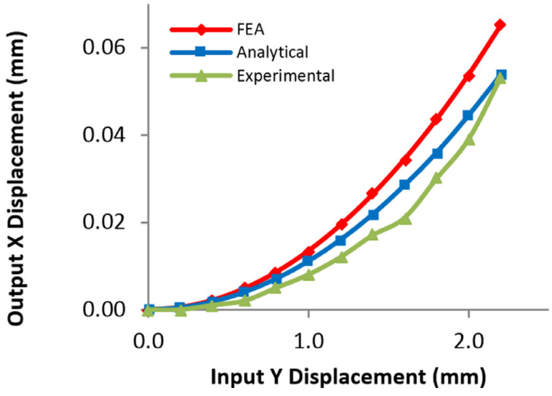

Fig. 15. Parasitic displacement for single direction loading.

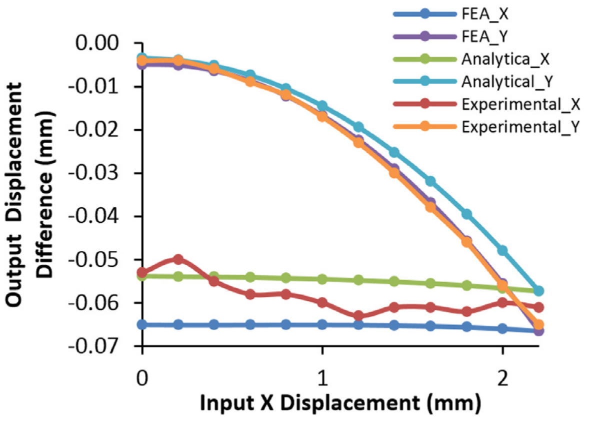

Fig. 16. Input/output displacement difference after applying a preload along the *Y*-axis.

along the *X*-axis is shown in Fig. 15. The maximum parasitic displacement from the analytical model is 54 µm while it is 65 µm from FEA, corresponding to an error of 17%.

Then, while keeping the input displacement along the *Y*-axis at 2.2 mm, an input displacement of 2.2 mm is gradually applied at point *D* along the *X*-axis. The difference between the input and output displacements along both directions are shown in Fig. 16. The first observation made is that the parasitic displacement along the *X*-axis caused by the preload is almost constant for both FEA and the analytical model. The second observation is that the input/output displacement difference along both directions is the same for FEA and the analytical model, with less than 0.5% error. The nonlinear model can therefore accurately predict cross-coupling and loss motion and can therefore be included in the control system for error compensation.

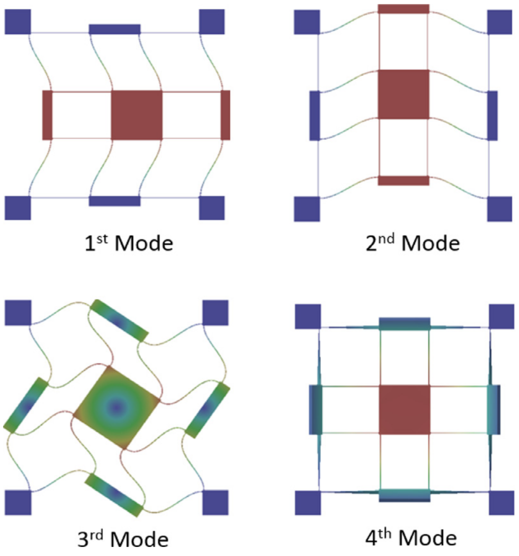

Fig. 17. Modal analysis results from FEA.

Table 3
Resulting resonant frequencies.

	Mode 1 (*X*)	Mode 2 (*Y*)	Mode 3 (??)	Mode 4 (*Z*)
FEA (Hz)	55.8	55.9	249.5	313.3
Analytical (Hz)	54.7	54.9	269.7Hz	353.8
Experimental (Hz)	47	47	–	267

5.5. *Modal analysis*

A dynamic analysis of the stage is carried out with ABAQUS using the Lanczos Eigen solver. The mass of the accelerometer (8 g) is added to the model. The results are shown in Fig. 17 and Table 3. The first two modes correspond to simultaneous vibrations along both the *X*- and *Y*-axes, which occurs at 55.8 Hz. The third mode, corresponding to a rotation around the *Z*-axis occurs at 249.5 Hz. Finally, the fourth mode, corresponding to vibrations along the *Z*-axis, occurs at a frequency of 313.3 Hz. Comparing the results from the analytical model (Eq. (59)) with the FEA results, the error for the first two modes is 1.9%, 8.1% for the third mode and 12.9% fourth mode.

The reason why the dynamic model shows larger errors for higher modes is that it represents the stage as a single 6-DOF element. One solution to this issue could be to model the *XY* stage a multi-DOF system, with each link (i.e. parallelograms *A, B, C, D* and *O*) free to undergo 6-DOF motion. In addition, the boundary conditions of a fixed-guided beam are accurate for bending but introduce some error when the beams are twisting. However, this model is sufficient for an accurate estimate of the first three modes, which is sufficient for the design of motion stage.

6. Experimental validation

In order to verify the theoretical characteristics of the *XY* micro-motion stage, a prototype is fabricated using Wire Electric Discharge Machining (WEDM). Corners of 0.5 mm radius have been added to reduce the stress concentration. The stage is driven by two VCAs from Moticont (LVCM-051-064-02) with a 12.7 mm stroke, 68.2 N continuous force and a force constant of 21.6 N/A. They are controlled by two Ingenia Pluto Drives, allowing for a position command resolution of 1.12 µm over ±2.3 mm along both directions. The input displacement of the *XY* motion stage is measured using two linear encoders from

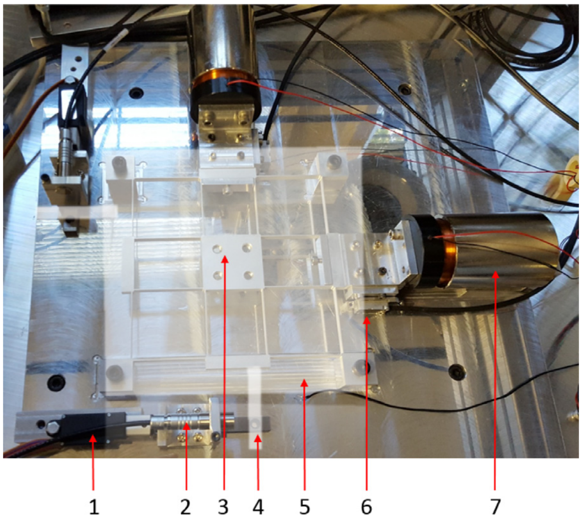

Fig. 18. Fabricated *XY* stage. (1) Linear actuator, (2) capacitive sensor head, (3) compliant *XY* stage, (4) target, (5) moving platform, (6) linear encoder, (7) VCA.

Renishaw (ATOM4T0-150) with a resolution of 100 nm. The output displacement is measured with two capacitive sensor heads (CS1) from Micro-Epsilon with DT6110 controllers, giving a resolution of 100 nm and an accuracy of reading of 0.5 µm over a range of 1 mm. These sensors are mounted on a carrier and are moved along a guiding rail using two Firgelli L12-P micro linear actuators with a 10 mm stroke and ±0.1 mm repeatability. The assembled stage is presented in Fig. 18.

6.1. Force-displacement test

In order to validate the analytical model a test is carried out to establish the relationship between the input displacement and the actuation force. The input displacement along the *X*-axis it maintained at 0 mm while it is varied from 0 mm to 2 mm along the *Y*-axis. The linear encoders are used to measure the position. As the servo drives include a built-in current sensor, the force is derived from the current using the VCA's force constant. The results are shown in Fig. 10. The force error of the first few readings is due to the internal friction in the bearings and can be neglected.

The maximum force error, occurring at 2 mm, is 11.1% when compared with FEA and 3.9% when compared with the analytical model. FEA is assumed to be the most accurate prediction for an ideal system while the fabricated stage behaves in a slightly different way, giving the impression that the analytical model is more accurate than FEA. This can be explained by the simplifications made in the nonlinear model and by the manufacturing and assembly tolerances affecting the fabricated stage meaning that both deviate from FEA.

6.2. Coupling test

A coupling analysis is carried out by first applying an input displacement of 2.2 mm along the *Y*-axis and recording the parasitic displacement along the *X*-axis. Following this, an input displacement of 2.2 mm is applied along the *X*-axis and the output displacements are recorded. The maximum recorded parasitic displacement for a single direction loading (Fig. 15) is 53 µm, corresponding to an error of 18.5% when compared to FEA and 1.9% when compared to the analytical model. When loading along both directions, the difference between the input and the output displacements is 61 µm along the *X*-axis and 65 µm along the *Y*-axis. This corresponds to a maximum positioning error of 0.3% when compared with FEA and 0.4% when compared with the analytical model. This confirms the FEA results proving that the nonlinear model can accurately predict the displacement error caused by cross-coupling and motion loss.

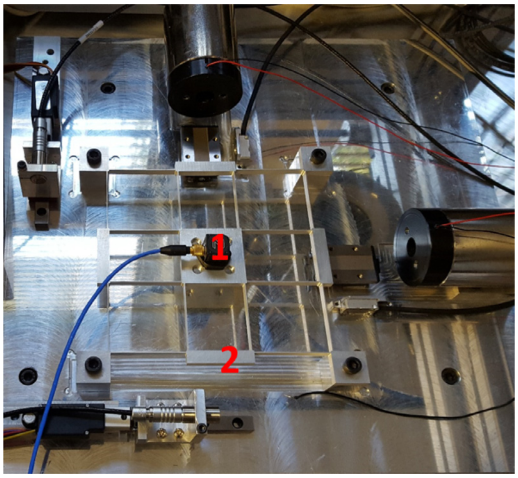

Fig. 19. Experimental vibration test setup. (1) 3D accelerometer, (2) compliant *XY* stage.

The output displacement error along the *X*-axis caused by the cross-coupling is 53 µm and the maximum lost motion recorded along the *X*-axis is estimated by subtracting the cross-coupling error from the total displacement error, giving a motion loss of approximately 8 µm. This corresponds to a cross-coupling of less than 2.5% and a lost motion of less than 0.4%. As discussed in [39], these errors can be significantly reduced by connecting the parallelograms *A* and *C* and the parallelograms *B* and *D* together. However, this would make the design bulkier and also make the assembly of a platform to the centre of the stage complicated. Alternatively, the control system of the *XY* stage will integrate the presented nonlinear model to compensate the positioning error.

6.3. Frequency response

In order to obtain the frequency response of the *XY* motion stage, a testing rig is set up to generate vibrations with a hammer and measure the frequency response with a 3-dimensional accelerometer (ICP-T356A16) placed at the centre of the stage. The sensitivity of the accelerometer is 100 mV/G and its output signal is processed by a Dual Channel Accelerometer Amplifier (FE-376-IPF) and acquired by a Data Acquisition card from National Instruments. Labview is used to obtain the frequency domain response using Fast Fourier Transform (FFT). The sampling rate is 10 kHz. The testing rig setup is presented in Fig. 19. The recorded resonant frequencies are 47 Hz along the *X*- and *Y*-axes and 267 Hz along the *Z*-axis (Table 3). When compared with FEA, the corresponding errors are 15.8% and 14.8% along the *X*- and *Y*-axes and the *Z*-axis respectively.

When comparing with the analytical model, the errors are 14.4% and 24.5%. This error can be due to the mounts applying a small preload in the beams when being screwed. One limitation of the analytical dynamic model is its ability to predict accurately high order resonant frequencies. However, this has a limited impact on the design optimisation results and on the performances of the fabricated motion stage.

7. Conclusions

An analytical model combining a linear and a simplified nonlinear model was presented. The combination of these two models was implemented in MATLAB to fully characterise and optimise an *XY* micro-motion stage. From this model, a compliant *XY* micro-motion stage was developed. The results from FEA and experimental testing clearly show that the analytical model is an accurate characterisation of the behaviour of the stage in terms of stiffness and working range, taking into account limitations such as nonlinear buckling and stress. Furthermore, its ability to accurately predict the output displacement as a function of the input displacement makes it suitable for position control without necessarily needing a feedback loop. This model can be easily adapted to any compliant mechanism composed of basic compound parallelogram structures. The computation time required to perform design optimisation was within 140 s. The designed micro-motion stage has a cross-coupling of less than 2.5%, a travel range of ±2.3 mm^2 and a theoretical ratio between the first two and the third resonant frequency larger than 1/4.

The micro-motion stage will be used as the fine positioning mechanism of a hybrid mini-assembly system. Further studies will be carried out to include fatigue life in the design criteria and the stress concentration factors will be refined to improve the maximum displacement estimation.

Acknowledgements

The authors would like to thank the financial support from the Engineering and Physical Sciences Research Council (EPSRC), UK under grant no. EP/K018345/1.

References

[1] W. Dong, L.N. Sun, Z.J. Du, Design of a precision compliant parallel positioner driven by dual piezoelectric actuators, Sens. Actuators 135 (2007) 250–256.

[2] K.-B. Choi, J.J. Lee, Analysis and design of linear parallel compliant stage for ultra–precision motion based on 4-PP flexural joint mechanism, in: Proceeding of the International Conference on Smart Manufacturing Application (ICSMA), 2008, pp. 35–38.

[3] S. Lin, Y. Jia, I.P. Lei, Q. Xu, Design and optimization of a long-stroke compliant micropositioning stage driven by voice coil motor, in: Proceeding of the 12th International Conference on Control Automation Robotics & Vision (ICARCV), 2012, pp. 1716–1721.

[4] Q. Qi, R. Du, A vision based micro-assembly system for assembling components in mechanical watch movements, Proceeding of the International Symposium on Optomechatronic Technologies (ISOT), 2010.

[5] E.D. Kunt, A.T. Naskali, I.S.M. Khalil, A. Sabanovic, E. Yüksel, Design and development of workstation for microparts manipulation and assembly, Turk. J. Electr. Eng. Comput. Sci. 19 (2011) 973–992.

[6] Y. Li, Q. Xu, Design and analysis of a totally decoupled flexure-based XY parallel micromanipulator, IEEE Trans. Robot. 25 (2009) 645–657.

[7] H. Tang, Y. Li, Design, analysis, and test of a novel 2-DOF nanopositioning system driven by dualmode, IEEE Trans. Robot. 29 (2013) 650–662.

[8] X. Yang, W. Li, Y. Wang, L. Zhang, G. Ye, X. Su, Analysis of the displacement of complaint double parallel fourbar mechanism, in: Proceeding of the IEEE Conference on Industrial Electronics and Applications (ICIEA), 2009, pp. 2760–2763.

[9] G. Hao, J. Yu, A completely kinematostatically decoupled XY compliant parallel manipulator through new topology structure, in: Proceedings of the IFToMM Workshop on Fundamental Issues and Future Research Directions for Parallel Mechanisms and Manipulators, 2014.

[10] Y. Li, J. Huang, H. Tang, A compliant parallel XY micromotion stage with complete kinematic decoupling, IEEE Trans. Autom. Sci. Eng. 9 (2012) 538–553.

[11] K.-B. Choi, D.-H. Kim, Monolithic parallel linear compliant mechanism for two axes ultraprecision linear motion, Rev. Sci. Instrum. 77 (2006) 065106.

[12] Y. Li, Z. Wu, Design, analysis and simulation of a novel 3-DOF translational micromanipulator based on the PRB model, Mech. Mach. Theory 100 (2016) 235–258 6//.

[13] L.-J. Lai, G.-Y. Gu, L.-M. Zhu, Design and control of a decoupled two degree of freedom translational parallel micro-positioning stage, Rev. Sci. Instrum. 83 (2012) 045105.

[14] Y. Tian, B. Shirinzadeh, D. Zhang, Design and dynamics of a 3-DOF flexure-based parallel mechanism for micro/nano manipulation, Microelectron. Eng. 87 (2010) 230–241.

[15] S. Xiao, Y. Li, Design and analysis of a novel flexure-based XY micro-positioning stage driven by electromagnetic actuators, in: Proceeding of the International Conference on Fluid Power and Mechatronics, 2011, pp. 953–958.

[16] J. Yu, Y. Xie, Z. Li, G. Hao, Design and experimental testing of an improved large-range decoupled XY compliant parallel micromanipulator, J. Mech. Robot. 7 (2015) 044503.

[17] G. Hao, X. Kong, A novel large-range XY compliant parallel manipulator with enhanced out-of-plane stiffness, J. Mech. Des. 134 (2012) 061009.

[18] Q. Xu, New flexure parallel-kinematic micropositioning system with large workspace, IEEE Trans. Robot. 28 (2012) 478–491.

[19] G. Hao, Q. Meng, and Y. Li, Design of large-range XY compliant parallel manipulators based on parasitic motion compensation, in: Proceedings of the ASME International Design Engineering Technical Conferences & Computers and Information in Engineering Conference (IDETC/CIE), 2013.

[20] Y.K. Yong, S.S. Aphale, S.O.R. Moheimani, Design, identification, and control of a flexure-based XY stage for fast nanoscale positioning, IEEE Trans. Nanotechnol. 8 (2009) 46–54.

[21] G.Y. Gu, L.M. Zhu, C.Y. Su, H. Ding, S. Fatikow, Modeling and control of piezo-actuated nanopositioning stages: a survey, IEEE Trans. Autom. Sci. Eng. 13 (2016) 313–332.

[22] L.L. Howell, A. Midha, A method for the design of compliant mechanisms with small-length flexural pivots, J. Mech. Des. 116 (1994) 280–290.

[23] B. Deshmukha, S. Pardeshib, R. Mistrya, S. Kandharkarb, S. Waghb, Development of a four bar compliant mechanism using pseudo rigid body model (PRBM), Proc. Mater. Sci. 6 (2014) 1034–1039.

[24] D.C. Handley, T.-F. Lu, Y.K. Yang, C. Eales, Workspace investigation of a 3 DOF compliant micro-motion stage, in: Proceeding of the ICARCV International Conference on Control, Automation, Robotics and Vision, 2004, pp. 1279–1284.

[25] O.A. Turkkan, H.J. Su, DAS-2D: a concept design tool for compliant mechanisms, Mech. Sci. 7 (2016) 135–148.

[26] V. Kalpathy Venkiteswaran, H.-J. Su, A 3-spring pseudo-rigid-body model for soft joints with significant elongation effects, J. Mech. Robot. (2016).

[27] V.K. Venkiteswaran, H.-J. Su, A parameter optimization framework for determining the pseudo-rigid-body model of cantilever-beams, Precis. Eng. 40 (2015) 46–54 4//.

[28] Y. Zhang, H.-J. Su, Q. Liao, Mobility criteria of compliant mechanisms based on decomposition of compliance matrices, Mech. Mach. Theory 79 (2014) 80–93 9//.

[29] H.-J. Su, H. Shi, J. Yu, A symbolic formulation for analytical compliance analysis and synthesis of flexure mechanisms, J. Mech. Des. 134 (2012) 051009.

[30] Y. Li, S. Xiao, L. Xi, Z. Wu, Design, modeling, control and experiment for a 2-DOF compliant micro-motion stage, Int. J. Precis. Eng. Manuf. 15 (2014) 735–744.

[31] H. Shi, H.-J. Su, N. Dagalakis, A stiffness model for control and analysis of a MEMS hexapod nanopositioner, Mech. Mach. Theory 80 (2014) 246–264 10//.

[32] J. Shang, Y. Tian, Z. Li, F. Wang, K. Cai, A novel voice coil motor-driven compliant micropositioning stage based on flexure mechanism, Rev. Sci. Instrum. 86 (2015) 095001.

[33] G. Hao and X. Kong, Novel XY compliant parallel manipulators for large displacement translation with enhanced stiffness, in: Proceedings of the ASME International Design Engineering Technical Conferences & Computers and Information in Engineering Conference (IDETC/CIE), 2010.

[34] Q. Xu, Design and testing of a novel XY micropositioning stage with dual ranges and resolutions, in: Proceeding of the IEEE International Conference on Robotics and Automation (ICRA), 2014, pp. 2351–2356.

[35] Q. Xu, A modular two-axis compliant parallel micropositioning stage with long travel range, in: Proceeding of the IEEE International Conference on Information and Automation (ICIA), 2013, pp. 898–903.

[36] Y. Shimizu, Y. Peng, J. Kaneko, T. Azuma, S. Ito, W. Gao, et al., Design and construction of the motion mechanism of an XY micro-stage for precision positioning, Sens. Actuators A 201 (2013) 395–406.

[37] P.M. Moore, M. Rakotondrabe, C. Clevy, G.J. Wiens, Development of a modular compliant microassembly platform with integrated force measurement capabilities, Proceeding of the 7th International Conference on MicroManufacturing (ICOMM), 2012.

[38] G. Hao, Extended nonlinear analytical models of compliant parallelogram mechanisms: third-order models, Trans. Can. Soc. Mech. Eng. 39 (2014) 71–83.

[39] G. Hao, J. Yu, Design, modelling and analysis of a completely-decoupled XY compliant parallel manipulator, Mech. Mach. Theory (2016).

[40] G. Hao, H. Li, Extended static modeling and analysis of compliant compound parallelogram mechanisms considering the initial internal axial force, J. Mech. Robot. 8 (2016) 041008.

[41] G. Hao, H. Li, Nonlinear analytical modeling and characteristic analysis of a class of compound multibeam parallelogram mechanisms, J. Mech. Robot. 7 (2015) 041016.

[42] S. Awtar, A.H. Slocum, E. Sevincer, Characteristics of beam-based flexure modules, J. Mech. Des. 129 (2006) 625–639.

[43] A. Zhang, G. Chen, A comprehensive elliptic integral solution to the large deflection problems of thin beams in compliant mechanisms, J. Mech. Robot. 5 (2013) 021006.

[44] Y. Koseki, T. Tanikawa, N. Koyachi, T. Arai, Kinematic analysis of translational 3-DOF micro parallel mechanism using matrix method, in: Proceeding of the IEEE/RSJ International Conference on Intelligent Robots and Systems, vol. 1, 2000, pp. 786–792.

[45] R.G. Budynas, J.K. Nisbett, Deflection and stiffness, in: Shigley's Mechanical Engineering Design, ninth ed., McGraw-Hill, New York, 2011, pp. 148–191.

[46] M. Vable, Mechanics of Materials, second ed., Oxford University Press, Oxford, UK, 2010.

[47] S. Timoshenko, D. Young, Vibration Problems in Engineering, D van Nostrand Company, Inc., New-York, 1937.

[48] D. Zhang, Z. Gao, I. Fassi, Design optimization of a spatial hybrid mechanism for micromanipulation, Int. J. Mech. Mater. Des. 7 (2011) 55–70.

[49] S. Xiao, Y. Li, Optimal design, fabrication, and control of an XY micropositioning stage driven by electromagnetic actuators, IEEE Trans. Ind. Electron. 60 (2013) 4613–4626.